Magnetic proximity and nonreciprocal current switching in a monolayer WTe_2 helical edge

Wenjin Zhao[1], Zaiyao Fei[1], Tiancheng Song[1], Han Kyou Choi[1], Tauno Palomaki[1], Bosong Sun[1], Paul Malinowski[1], Michael A. McGuire[3], Jiun-Haw Chu[1], Xiaodong Xu[1,2*], David H. Cobden[1*]
[1]Department of Physics, University of Washington, Seattle, WA, USA
[2]Department of Materials Science and Engineering, University of Washington, Seattle, WA, USA
[3]Materials Science and Technology Division, Oak Ridge National Laboratory, Oak Ridge, TN, USA
[*]Corresponding authors: cobden@uw.edu, xuxd@uw.edu

Abstract:

The integration of diverse electronic phenomena, such as magnetism and nontrivial topology, into a single system is normally studied either by seeking materials that contain both ingredients, or by layered growth of contrasting materials[1-9]. The ability to simply stack very different two-dimensional (2D) van der Waals materials in intimate contact permits a different approach[10-12]. Here we use this approach to couple the helical edges states in a 2D topological insulator, monolayer WTe_2[13-17], to a 2D layered antiferromagnet, CrI_3[18]. We find that the edge conductance is sensitive to the magnetization state of the CrI_3, and the coupling can be understood in terms of an exchange field from the nearest and next-nearest CrI_3 layers that produces a gap in the helical edge. We also find that the nonlinear edge conductance depends on the magnetization of the nearest CrI_3 layer relative to the current direction. At low temperatures this produces an extraordinarily large nonreciprocal current that is switched by changing the antiferromagnetic state of the CrI_3.

Main Text:

The introduction of magnetic order into topological band structure gives rise to new phenomena such as the quantum anomalous Hall effect[1,8,9] and nonreciprocal magnetoelectric effects[5-7,19]. In the case of a two-dimensional topological insulator (2D TI), topology guarantees the existence of helical edge modes in which the spin is locked to momentum, causing current at the edge to be fully spin-polarized (the quantum spin Hall effect)[20-22]. Combining 2D TIs with magnets should therefore directly yield magnetoelectric coupling[23,24]. For example, a magnetic proximity effect may modify the spin polarization and hence the current, or the flow of current in the edge may produce a torque on the magnetization[25,26]. Since backscattering in the edge modes is suppressed by time reversal symmetry, the edge conduction should be affected by magnetic order, which will mix the two opposite-spin branches and so modify backscattering. The expected gapping of the helical edge modes by proximity with a ferromagnet is an important way to control them which, combined with induced superconductivity[27,28], plays a role in schemes to produce Majorana modes[29].

Stacking van der Waals materials offers a simple, flexible and low-disorder approach to combining magnets with other materials[10-12]. In this work we measure transport through a 2D TI, monolayer (1L) WTe_2[14-17], stacked under the layered magnetic insulator CrI_3[18,30-34]. We find that the magnetism of the CrI_3 suppresses the edge conduction in the WTe_2, in a manner consistent with the opening of a gap by an exchange field. The linear edge conductance is sensitive to the magnetization state of the CrI_3, and changes suddenly when the magnetization of the nearest or next-nearest CrI_3 layer flips. In addition, the nonlinear current-voltage characteristic has an even component that changes sign when the magnetization of the adjacent CrI_3 layer reverses. This is

related to the "unidirectional magnetoresistance" seen in magnetically doped 3D TI structures where it was explained by spin-flip scattering of electrons by magnons[5,6]. However, in the helical edge at low temperatures the effect exists at zero external field and can be extremely large, creating a difference in (nonreciprocal) current of order 100% between the two opposite antiferromagnetic ground states of the CrI_3.

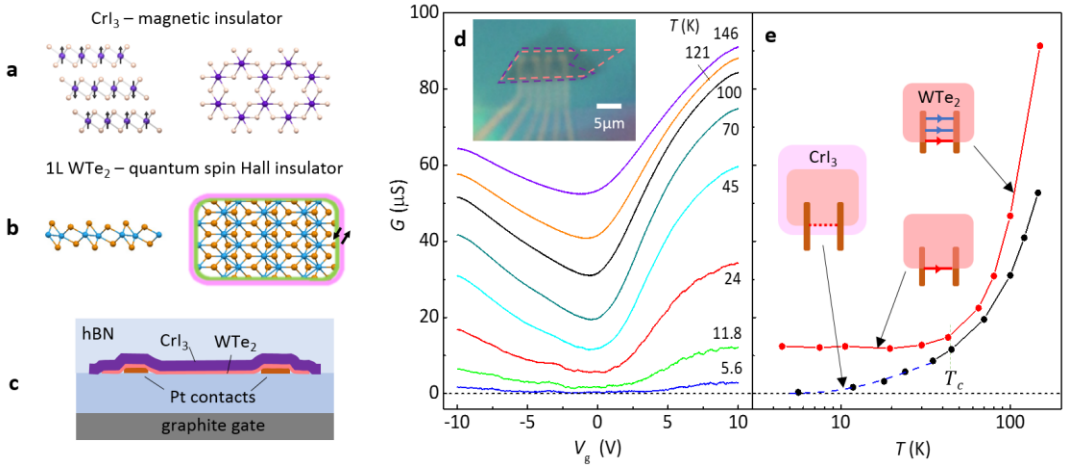

Figure 1. Characteristics of a CrI_3/WTe_2 device with no applied field. a, Side view indicating the layered antiferromagnetic order in CrI_3 below $T_c \approx 45$ K, and top view of monolayer structure (Cr: purple, I: yellow). **b,** Side and top views of the structure of monolayer (1L) WTe_2 (W: blue, Te: orange). The presence of helical edge states is indicated in cartoon form. **c,** Schematic device cross-section. **d,** Gate dependence of the linear conductance between two adjacent contacts (separated by 0.8 μm) at different temperatures for device C1, which has trilayer CrI_3. The capacitively induced doping per gate voltage is 1.2×10^{12} cm^{-2}/V. Inset: optical image of device C1; the trilayer CrI_3 and 1L WTe_2 flakes are outlined by purple and pink dashed lines, respectively. **e,** Temperature dependence of the minimum conductance for device C1 (black) and for bare (no CrI_3) 1L WTe_2 device M1 (red). The insets indicate the relevance of bulk and edge currents in each case.

The structure and magnetic configuration of CrI_3 at zero magnetic field is indicated in Fig. 1a. Each layer is internally ferromagnetic, with the moments aligned out of the plane below a critical temperature of $T_C \approx 45$ K. In thin exfoliated CrI_3 flakes, adjacent layers are antiferromagnetically coupled and thus have opposite magnetization. The structure of 1L WTe_2 is sketched in Fig. 1b. Although semi-metallic at room temperature or when doped, below ~100 K and at low gate voltages the 2D bulk shows insulating behavior while the edge remains conducting. Both theory[13] and experiments[14-17] indicate that the edge states are helical (signified by the green and pink bordering lines representing the two spins channels), i.e., this is a quantum spin Hall system. For example, the edge conductance is strongly suppressed by an in-plane magnetic field. Each of our devices contains a monolayer flake of WTe_2 that is either partly or completely covered by a few-layer flake of CrI_3, as sketched in Fig. 1c. The WTe_2 overlies prepatterned platinum contacts, all encapsulated between two hexagonal boron nitride (hBN) dielectric layers, with a graphite bottom gate to which a gate voltage V_g is applied (Supplementary SI-1).

Figure 1d shows the V_g dependence of the linear-response conductance G measured between two adjacent contacts in device C1, which has trilayer CrI_3 covering most of the WTe_2 (see the inset optical image). G exhibits a minimum near $V_g = 0$. The value at the minimum, plotted vs T in Fig. 1e (black points), decreases monotonically on cooling. Above about 50 K the behavior is similar to that of a typical bare 1L WTe_2 device M1 (red points), in which the bulk conductivity steadily decreases. However, at lower temperatures in the bare device the conductance levels off due to temperature-independent edge conduction, whereas in C1 it continues to drop to the lowest

temperature of 5.6 K. Similar behavior was seen in four devices whenever CrI_3 covered at least part of the edge in the current path (Supplementary SI-2 and SI-3). The blue dashed line is an Arrhenius fit of the form $G \propto \exp(-E_a/k_BT)$ to the data in this regime, where k_B is Boltzmann's constant, yielding an activation energy $E_a = 2.5 \pm 0.3$ meV. This is consistent with the idea that coupling to the magnet opens a gap E_a in the helical edge mode. A theory of this suppression that takes into account the combined effects of disorder, magnetism and electron-electron interactions is not available at present. We therefore focus here on the effects of changing the magnetization state of the CrI_3 using a perpendicular magnetic field B.

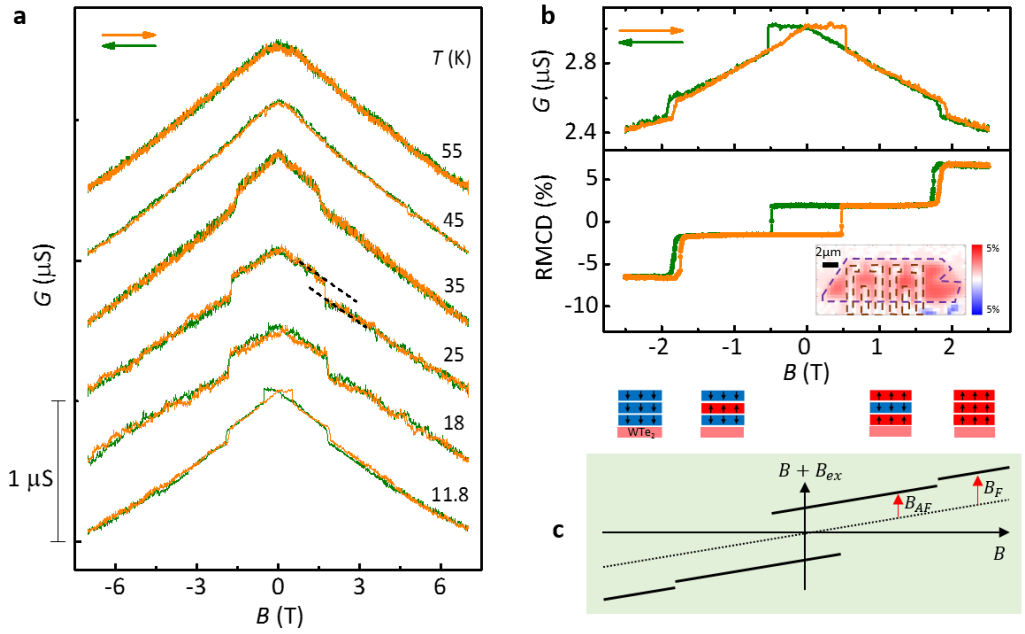

Figure 2. Conductance jumps and magnetic state changes in an applied magnetic field. a, Linear conductance (measured using 1 mV ac bias) vs. out-of-plane magnetic field B at $V_g = -0.5$ V for device C1 at the indicated temperatures. The dashed lines indicate the effective shift of the characteristic that occurs at one of the jumps (see text). The traces are vertically offset for clarity; the conductance at $B = 0$ can be read off Fig. 1e. **b**, Upper: conductance, and lower: RMCD signal as a function of B (10 mV ac bias, $V_g = -1$ V, T =11.8 K). Inset: spatial map of RMCD signal at $B = 0$ after reducing B from +2.5 T. The boundaries of the Pt contacts and trilayer CrI_3 are indicated by purple and yellow dashed lines, respectively. Beneath are schematics of the corresponding magnetic states of the trilayer CrI_3 (blue and red for down and up polarizations) atop 1L WTe_2 (pink). **c**, Schematic variation of the sum of the real and exchange magnetic fields used to interpret the behavior of G in panel b.

Figure 2a shows the linear conductance of device C1 as B is swept upwards (orange) and downwards (green) at a series of temperatures, measured at a gate voltage (V_g = -0.5 V) where edge conduction dominates. To within the noise the upwards traces are the same as the downwards traces reflected in $B = 0$, as should be the case by time-reversal considerations. At temperatures above T_c~45 K, G decreases smoothly with increasing B as does the edge conduction in bare WTe_2. Below 45 K a jump appears in the vicinity of $\pm$1.8 T, and at lower temperatures a second jump becomes visible at around $\pm$ 0.5 T. The positions of the jumps are not affected by V_g (Supplementary SI-4) or by current in the WTe_2. Figure 2b compares the conductance (upper panel) with the reflection magnetic circular dichroism (RMCD) signal (lower panel) measured on the same device at 11.8 K (for more temperatures, see Supplementary SI-5). The RMCD signal is roughly proportional to the total out-of-plane magnetization, and the plateaus in it correspond to the four magnetization states of trilayer CrI_3 indicated by the schematics beneath. The inset to Fig. 2b is a

2D map of the RMCD signal taken at $B = 0$ during a downwards sweep of B. Its uniformity implies that there is a single magnetic domain over most of the WTe_2.

It is clear that the conductance jumps occur when the magnetic state of the CrI_3 changes. The higher-field jumps accompany transitions between antiferromagnetic (AF) and fully polarized (F) states, which we refer to $\downarrow\uparrow\downarrow - \downarrow\downarrow\downarrow$ and $\uparrow\downarrow\uparrow - \uparrow\uparrow\uparrow$, where the last arrow represents the polarity of the lowest layer, the one in contact with the WTe_2. Such spin-flip transitions have little hysteresis. The lower-field jumps accompany transitions between the two antiferromagnetic states, $\downarrow\uparrow\downarrow - \uparrow\downarrow\uparrow$. They show larger hysteresis because the magnetic reconfiguration is more drastic.

The sizes and signs of the conductance jumps are consistent with a simple model in which the WTe_2 conduction electrons experience a perpendicular exchange magnetic field, B_{ex}, that adds to the external field so that the conductance becomes $G_0(B + B_{ex})$, where $G_0(B)$ is conductance without the CrI_3. We assume B_{ex} takes values $\pm B_F$ for $\uparrow\uparrow\uparrow$ and $\downarrow\downarrow\downarrow$, and $\pm B_{AF}$ for $\uparrow\downarrow\uparrow$ and $\downarrow\uparrow\downarrow$, respectively. The variation of $B + B_{ex}$ with B is sketched in Fig. 2c. In this model the higher-field jump is between $G_0(B + B_{AF})$ and $G_0(B + B_F)$. Since $G_0(B)$ is roughly linear with similar slope on either side of this jump, as indicated by the dashed lines drawn on the 25 K data in Fig. 2a, we can use the separation of these lines to estimate $B_F - B_{AF} \approx +1$ T. The lower-field jump, which should be between $G_0(B_{AF} + B)$ and $G_0(B - B_{AF})$, cannot be analyzed so simply, but making use of the Onsager symmetry $G_0(B) = G_0(-B)$ we can infer that B_{AF} is much larger than the coercive field, putting it at several Tesla (Supplementary SI-6). If we interpret the activation energy for the edge (Fig. 1e) as a Zeeman-like gap induced by B_{AF}, i.e., $E_a \approx g\mu_B B_{AF}$, and use a g-factor of $g = 4$ estimated from the magnetoresistance (Supplementary SI-7), we obtain B_{AF}~10 T, where μ_B is Bohr magneton. This is similar in magnitude to the exchange field of 13 T found in CrI_3/WSe_2 heterostructures[10].

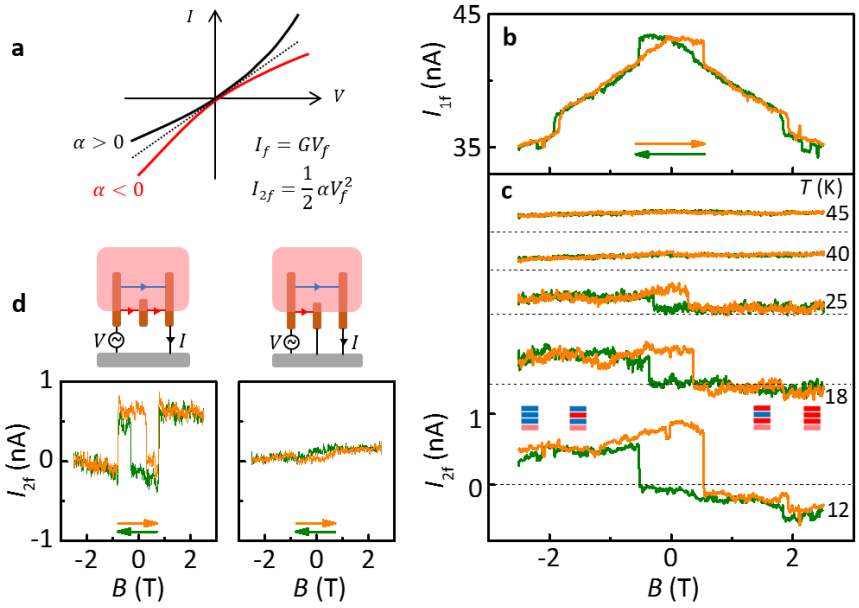

Figure 3. Nonlinear current measurements. a, Sketch indicating the relationship of the first- and second-harmonic current components to the asymmetry in the $I - V$ which is parameterized by quadratic coefficient α. **b**, I_f vs B for device C1 at $V_g = -0.5$ V and $T = 12$ K with ac voltage bias V_f =15 mV. **c**, I_{2f} vs B measured under the same conditions (lowest traces) and at several other temperatures as labelled. The traces are vertically offset for clarity and the dashed horizontal lines show the zero level for each temperature. The schematics are repeated from Fig. 2c. **d**, Second harmonic current vs B for device C3 at $V_g = 0.1$ V, $T = 27$ K and V_f =100 mV, compared between the two different measurement configurations as indicated. Bulk and edge currents are signified by blue and red arrows respectively.

We next investigate the nonlinear conductance, which yields additional information since it is not constrained by the Onsager symmetry imposed by near-equilibrium conditions. We begin by working at higher temperatures where the linear conductance G is measurable. We apply an ac bias of rms amplitude V_f at frequency f and measure the resulting ac current components at f and $2f$, with V_f chosen such that $I_{2f} << I_f$. If we write $I = GV + \alpha V^2 + \cdots$ then $I_f = GV_f$, and $I_{2f} = \alpha V_f^2/2$ is proportional to the coefficient α which parameterizes the conductance asymmetry between positive and negative bias directions, as indicated in Fig. 3a. Measurements of I_f vs B for device C1, shown in Fig. 3b, match the ac linear conductance measurements in Fig. 2a as expected, exhibiting four jumps. Measurements of I_{2f} at several temperatures, plotted in Fig. 3c, show large jumps corresponding to the $\uparrow\downarrow\uparrow - \downarrow\uparrow\downarrow$ transitions, detectable up to 40 K, but no discernable features at the $\downarrow\downarrow\downarrow - \downarrow\uparrow\downarrow$ or $\uparrow\uparrow\uparrow - \uparrow\downarrow\uparrow$ transitions in which the magnetization of the lowest layer does not flip (Supplementary SI-8, SI-9 and SI-10). We conclude that the asymmetry parameter α is sensitive to the magnetization of the nearest layer of CrI_3 but not to that of the next nearest layer.

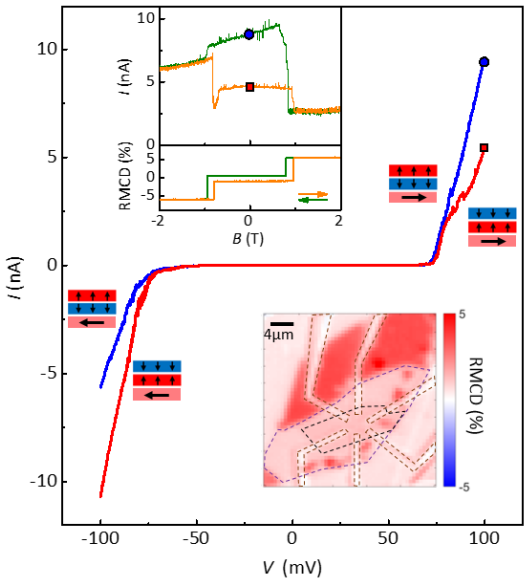

Figure 4. Large nonreciprocal current controlled by the antiferromagnetic state. *I-V* traces at zero magnetic field at 1.6 K and $V_g = 0$ V for device C2, which has bilayer CrI_3. The schematics indicate the magnetization state of the CrI_3 and the current flow direction in the 1L WTe_2. Upper inset: current at 100 mV dc bias (corresponding to the points marked with symbols in the *I-V* traces) and RMCD signal vs magnetic field. Lower inset: spatial map of RMCD signal at 0 T after reducing from +2.5 T. The current is measured between the upper two contacts. The boundaries of bilayer CrI_3, Pt contacts, and WTe_2 are outlined with purple, dark yellow and black dashed lines, respectively.

In these nonlinear measurements the larger bias used may drive some current through the WTe_2 bulk, whose activation gap is ~50 meV[15], so we performed an experiment to test whether this bulk current is relevant. Figure 3d shows I_{2f} vs B for a large ac bias ($V_f = 100$ mV) applied to device C3, which has the contact pattern indicated in the sketches. In two-terminal measurements between the outer contact pair (left), I_{2f} shows large jumps. However, when the intervening contact is grounded (right) the jumps almost disappear. This implies that when current is prevented from flowing along the edge there is no sensitivity to the state of the CrI_3 (Supplementary SI-11). We deduce that in both nonlinear and linear regimes the sensitivity to the magnetic state of the CrI_3 is dominated by the sample edges.

Finally, we turn to the nonlinear behavior at lower temperatures, where the linear conduction freezes out. Figure 4 shows two-terminal $I-V$ traces at 1.6 K for bilayer CrI_3 device C2 at $B=0$. No current is detected below a threshold bias of ~70 mV in either direction. Above this bias the current depends strongly on B and exhibits hysteresis between two stable states at low fields (upper inset). Correspondingly, either of the two different $I-V$ traces shown (blue and red) can be obtained. RMCD measurements (shown at the bottom of the upper inset) connect them with the two antiferromagnetic states, ↑↓ or ↓↑, of the bilayer CrI_3. An RMCD map taken at $B=0$ (lower inset) shows a uniform magnetic state over most of the WTe_2. A finite RMCD signal in the antiferromagnetic state, as seen here, is normal for CrI_3 bilayers[32-34] and implies uncompensated magnetization between the two layers, probably in this case related to contact with the WTe_2 (for more temperatures, see Supplementary SI-12 and SI-13). A transition to a fully polarized state (↑↑ or ↓↓) occurs at when B exceeds ≈ 0.9 T.

Inspection of Fig. 4 shows that in the ↑↓ state (blue) the current at positive bias is roughly double that at negative bias, i.e., it is strongly nonreciprocal. Importantly, in the ↓↑ state (red) the opposite is true, implying that the dominant part of the nonreciprocal current is connected to the orientation of the magnetization of the lowest CrI_3 layer relative to the current direction. This corresponds to the property of α mentioned above. A similar nonreciprocal resistance change on magnetization reversal was reported before in magnetic/nonmagnetic topological insulator thin-film heterostructure[5,6], though it was of modest size and vanished at zero applied field, being referred to as unidirectional magnetoresistance (UMR). Here, the nonreciprocal effect is orders of magnitude larger (at the 100% level) and is present at zero applied field.

A natural interpretation of relationship of the nonreciprocal current to the magnetization is analogous to the one put forward in Ref 5. Backscattering that opposes current flowing, say, to the right in the helical edge requires spin-flips from "up" to "down" (note that the actual spin alignment axis is presently unknown), and vice versa for current flowing in the opposite direction. The spin flip may be assisted by excitation of magnons within the nearest CrI_3 layer. These magnons carry spin opposite to the ferromagnetic polarization of that layer; therefore, one polarization allows more scattering of a right-flowing current, and the opposite allows more scattering of a left-flowing current. In this system the effect can be very large because no small-angle scattering is possible in the 1D helical edge, and also because there is little or no conduction in parallel through the bulk.

In summary, we have observed and studied coupling of the magnetism in insulating layered CrI_3 to the edge states of a quantum spin Hall insulator (monolayer WTe_2). The results are consistent with the edge states being helical (spin locked to momentum). The behavior of the linear edge conductance can be interpreted in terms of an exchange field of several Tesla which is dominated by the nearest layer of CrI_3 but is larger by ~ 1 T when the next nearest CrI_3 layer is polarized parallel (i.e., in the F state) than when it is antiparallel (in the AF state). The nonlinear conductance shows a large directional asymmetry that depends on the magnetization of only the nearest CrI_3 layer, and is thus highly sensitive to the AF ground state.

Acknowledgements: The authors acknowledge Lukasz Fidkowski and Di Xiao for insightful discussions. This project was supported by NSF DMR grants EAGER 1936697 and MRSEC 1719797. Materials synthesis at UW was partially supported by the Gordon and Betty Moore Foundation's EPiQS Initiative, Grant GBMF6759 to JHC. MAM was supported by the US Department of Energy, Office of Science, Basic Energy Sciences, Materials Sciences and Engineering Division.

Author Contributions: DC and XX conceived the experiment. WZ, ZF, HC, TP and BS fabricated the devices. WZ and ZF performed transport measurements. TS performed magnetic circular dichroism measurements. PM and JC grew the WTe_2 crystals. MM grew CrI_3 crystals. DC, WZ, XX and ZF wrote the paper with comments from all authors.

References:

1 Chang, C.-Z. *et al.* Experimental Observation of the Quantum Anomalous Hall Effect in a Magnetic Topological Insulator. *Science* **340**, 167, doi:10.1126/science.1234414 (2013).

2 Katmis, F. *et al.* A high-temperature ferromagnetic topological insulating phase by proximity coupling. *Nature* **533**, 513 (2016).

3 Wei, P. *et al.* Exchange-Coupling-Induced Symmetry Breaking in Topological Insulators. *Physical Review Letters* **110**, 186807, doi:10.1103/PhysRevLett.110.186807 (2013).

4 Avci, C. O. *et al.* Unidirectional spin Hall magnetoresistance in ferromagnet/normal metal bilayers. *Nature Physics* **11**, 570 (2015).

5 Yasuda, K. *et al.* Large Unidirectional Magnetoresistance in a Magnetic Topological Insulator. *Physical Review Letters* **117**, 127202, doi:10.1103/PhysRevLett.117.127202 (2016).

6 Fan, Y. *et al.* Unidirectional Magneto-Resistance in Modulation-Doped Magnetic Topological Insulators. *Nano Letters* **19**, 692-698, doi:10.1021/acs.nanolett.8b03702 (2019).

7 Lv, Y. *et al.* Unidirectional spin-Hall and Rashba−Edelstein magnetoresistance in topological insulator-ferromagnet layer heterostructures. *Nature Communications* **9**, 111, doi:10.1038/s41467-017-02491-3 (2018).

8 Deng, Y. *et al.* Magnetic-field-induced quantized anomalous Hall effect in intrinsic magnetic topological insulator $MnBi_2Te_4$. doi:arXiv:1904.11468 (2019).

9 Chang, L. *et al.* Quantum phase transition from axion insulator to Chern insulator in $MnBi_2Te_4$. *arXiv*, doi:arXiv:1905.00715 (2019).

10 Zhong, D. *et al.* Van der Waals engineering of ferromagnetic semiconductor heterostructures for spin and valleytronics. *Sci Adv* **3**, e1603113, doi:10.1126/sciadv.1603113 (2017).

11 Seyler, K. L. *et al.* Valley Manipulation by Optically Tuning the Magnetic Proximity Effect in WSe2/CrI3 Heterostructures. *Nano Letters* **18**, 3823-3828, doi:10.1021/acs.nanolett.8b01105 (2018).

12 Wei, P. *et al.* Strong interfacial exchange field in the graphene/EuS heterostructure. *Nature Materials* **15**, 711 (2016).

13 Qian, X., Liu, J., Fu, L. & Li, J. Quantum spin Hall effect in two-dimensional transition metal dichalcogenides. *Science* **346**, 1344-1347, doi:10.1126/science.1256815 (2014).

14 Fei, Z. *et al.* Edge conduction in monolayer WTe_2. *Nature Physics* **13**, 677-682, doi:10.1038/nphys4091 (2017).

15 Tang, S. *et al.* Quantum spin Hall state in monolayer 1T'-WTe_2. *Nat Phys* **13**, 683-687, doi:10.1038/nphys4174 (2017).

16 Wu, S. *et al.* Observation of the quantum spin Hall effect up to 100 kelvin in a monolayer crystal. *Science* **359**, 76-79, doi:10.1126/science.aan6003 (2018).

17 Shi, Y. *et al.* Imaging quantum spin Hall edges in monolayer WTe_2. *Science Advances* **5**, eaat8799, doi:10.1126/sciadv.aat8799 (2019).

18 Huang, B. *et al.* Layer-dependent ferromagnetism in a van der Waals crystal down to the monolayer limit. *Nature* **546**, 270-273, doi:10.1038/nature22391 (2017).

19 Tokura, Y. & Nagaosa, N. Nonreciprocal responses from non-centrosymmetric quantum materials. *Nature Communications* **9**, 3740, doi:10.1038/s41467-018-05759-4 (2018).

20 König, M. *et al.* Quantum Spin Hall Insulator State in HgTe Quantum Wells. *Science* **318**, 766-770, doi:10.1126/science.1148047 (2007).

21 Roth, A. *et al.* Nonlocal Transport in the Quantum Spin Hall State. *Science* **325**, 294-297, doi:10.1126/science.1174736 (2009).

22 Knez, I., Du, R.-R. & Sullivan, G. Evidence for Helical Edge Modes in Inverted InAs/GaSb Quantum Wells. *Physical Review Letters* **107**, 136603, doi:10.1103/PhysRevLett.107.136603 (2011).

23 Liu, C.-X., Qi, X.-L., Dai, X., Fang, Z. & Zhang, S.-C. Quantum Anomalous Hall Effect in $Hg_{1-y}Mn_yTe$ Quantum Wells. *Physical Review Letters* **101**, 146802, doi:10.1103/PhysRevLett.101.146802 (2008).

24 Gong, C. & Zhang, X. Two-dimensional magnetic crystals and emergent heterostructure devices. *Science* **363**, eaav4450, doi:10.1126/science.aav4450 (2019).

25 Liu, L. *et al.* Spin-Torque Switching with the Giant Spin Hall Effect of Tantalum. *Science* **336**, 555, doi:10.1126/science.1218197 (2012).

26 MacNeill, D. *et al.* Control of spin-orbit torques through crystal symmetry in WTe_2/ferromagnet bilayers. *Nature Physics* **13**, 300, doi:10.1038/nphys3933 (2017).

27 Sajadi, E. *et al.* Gate-induced superconductivity in a monolayer topological insulator. *Science* **362**, 922, doi:10.1126/science.aar4426 (2018).

28 Fatemi, V. *et al.* Electrically tunable low-density superconductivity in a monolayer topological insulator. *Science* **362**, 926, doi:10.1126/science.aar4642 (2018).

29 Fu, L. & Kane, C. L. Josephson current and noise at a superconductor/quantum-spin-Hall-insulator/superconductor junction. *Physical Review B* **79**, 161408 (2009).

30 Song, T. *et al.* Giant tunneling magnetoresistance in spin-filter van der Waals heterostructures. *Science* **360**, 1214, doi:10.1126/science.aar4851 (2018).

31 Klein, D. R. *et al.* Probing magnetism in 2D van der Waals crystalline insulators via electron tunneling. *Science* **360**, 1218, doi:10.1126/science.aar3617 (2018).

32 Huang, B. *et al.* Electrical control of 2D magnetism in bilayer CrI3. *Nature Nanotechnology* **13**, 544-548, doi:10.1038/s41565-018-0121-3 (2018).

33 Jiang, S., Li, L., Wang, Z., Mak, K. F. & Shan, J. Controlling magnetism in 2D CrI3 by electrostatic doping. *Nature Nanotechnology* **13**, 549-553, doi:10.1038/s41565-018-0135-x (2018).

34 Jiang, S., Shan, J. & Mak, K. F. Electric-field switching of two-dimensional van der Waals magnets. *Nature Materials* **17**, 406-410, doi:10.1038/s41563-018-0040-6 (2018).